International Journal of Disaster Risk Reduction 132 (2026) 105977

Contents lists available at ScienceDirect

International Journal of Disaster Risk Reduction

journal homepage: www.elsevier.com/locate/ijdrr

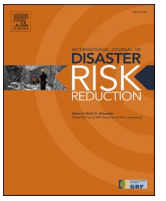

Earth observation informed modelling of flash floods

C. Scott Watson [a,*], Maggie Creed [b], Januka Gyawali [c], Sameer Shadeed [d], Jamal Dabbeek [d], Divya L. Subedi [e], Rojina Haiju [e]

[a] School of Geography and water@leeds, University of Leeds, LS2 9JT, UK
[b] James Watt School of Engineering, The University of Glasgow, Glasgow, G12 8QQ, UK
[c] Practical Action, Kathmandu, Nepal
[d] Civil and Architectural Engineering Department, An-Najah National University, Nablus, Palestine
[e] Water and Climate Program, Nepal Development Research Institute (NDRI), Lalitpur, Nepal

A B S T R A C T

More frequent extreme rainfall events in a changing climate increase the risk of flash flooding. However, the flood hazard modelling required to reduce disaster risk in urban environments is often limited by the availability of data required for model calibration and validation. Here, we use a historical flood event captured by 5 m resolution satellite imagery to inform future flood hazard assessments in the West Bank, Palestine. Flooding in January 2013 affected over 12,500 people and large areas of agricultural land. Vegetation loss and damage were captured using a normalised difference vegetation index (NDVI), which was used as a reference flood extent. The physics-based HEC-RAS flood model best reproduced this NDVI-derived inundation extent (F1 score = 0.76), although the FastFlood model was able to produce a similar inundation pattern (F1 score = 0.74) over 300 times faster. Simulated flood depths from both models were similar. Climate analysis revealed that the January 2013 rainfall corresponded to a historical return period of between 1 in 5 and 1 in 10 years. In comparison, a 1 in 100-year rainfall event (RX1day (maximum 1-day precipitation) of 148 mm) based on historical data (1985–2014) could increase by almost 40 % (to 205 mm) in the mid-future (2041–2060), which could cause 23 % (4 km^2) greater inundation compared to the 2013 event. Although the patterns of future precipitation in the region are uncertain, our flood hazard maps can support urban planning and infrastructure development to manage storm water runoff.

1. Introduction

A warming climate with more frequent extreme rainfall events [1,2] is coupled with increased exposure of populations and infrastructure to flooding [3–5]. Flood risk is driven by factors including higher magnitude flood events [6,7], human-modified catchment runoff characteristics [8], and encroachment into flood-prone areas [9,10]. The Intergovernmental Panel on Climate Change's Sixth Assessment Report (IPCC AR6) states that in many parts of Asia, the risks related to climate change are projected to increase progressively for 1.5 °C, 2 °C, and 3 °C of global warming [11]. Vulnerability to flooding, which is a function of physical, social, and economic factors, is generally highest in developing countries and informal settlements that lack planning and infrastructure to manage flood water [12,13]. Therefore, pro-poor risk-informed planning is essential to reduce flood risk in an equitable way for future developments [14,15]. However, robust flood modelling processes required to inform disaster risk reduction strategies require high-quality input data including future precipitation trends generated by analysing historical precipitation observations alongside global climate models [16,17]; an accurate digital elevation model that represents the channel and floodplain topography [18–20]; and data to calibrate and validate model outputs [21,22]. In developing countries, one or more of these inputs are often lacking. This can force simplifications to the modelling process and choice of flood model complexity, which can subsequently limit the

* Corresponding author.
E-mail address: c.s.watson@leeds.ac.uk (C.S. Watson).

https://doi.org/10.1016/j.ijdrr.2025.105977
Received 23 September 2025; Received in revised form 17 December 2025; Accepted 17 December 2025
Available online 24 December 2025

effectiveness of model outputs in decision making. For example, global flood hazard maps at ≥90 m resolution that use open access DEMs can provide valuable probabilistic hazard information at regional scales [23,24]. However, model intercomparisons highlight inconsistencies that are often linked to digital elevation model (DEM) resolution and accuracy, which affects how local channel and floodplain complexities are represented [18,25–27].

Earth observation data have broad applicability in flood disaster response and planning, owing to the large spatial coverage, frequent revisit times, and diversity of information provided by different sensors. For example, information on the duration and intensity of storms is available from precipitation monitoring missions such as NASA's Global Precipitation Measurement (GPM)[28,29]; the height of rivers and inundated land can be derived using satellite altimetry [30,31]; antecedent conditions including soil moisture can be obtained using radar [32,33]; flood routing and the effects on vegetation can be quantified using changing reflectance characteristics [34,35]; and inundation extents can be mapped using both optical and radar data [21,36–38]. Barriers to using earth observation datasets for city-scale flood hazard modelling include their availability and accessibility, since it is only within the last decade that spatial and temporal resolution has improved, alongside open access licensing. Additionally, the coarse resolution global satellite-derived products such as GPM may not capture the spatio-temporal complexities of precipitation and therefore the formation of flood peaks in flash flooding [39].

Reducing flood disaster risk requires knowledge of current and future flood hazards under realistic climate scenarios, combined with the ability to influence decision making at local scales. The Tomorrow's Cities project was designed to respond to this challenge through a risk-informed urban planning approach (Decision Support Environment (DSE)), weighted towards benefitting marginalised and vulnerable communities [14,40]. In this study, we aimed to draw on our experience in the application of the DSE in Nablus, Palestine, to evaluate established and emerging flood modelling approaches to demonstrate their applicability in a data-sparse flash flood environment. Our objectives were to: (1) quantify the impact of an extensive historical flood event using pre- and post-flood satellite imagery; (2) evaluate three flood hazard models of increasing complexity using the historical event for validation; and (3) use this to inform an assessment of current and future flood hazard in the region.

2. Study area

Our study focused on the north-western part of the West Bank, Palestine (in Jenin and Tulkarm governorates), which is thought to exhibit the greatest flood hazard, due to high rainfall and runoff potential [41](Fig. 1). In this region, increases in extreme rainfall, impermeable surfaces, and lack of infrastructure to deal with flood water have led to increasing vulnerability to flash floods [41–44]. A

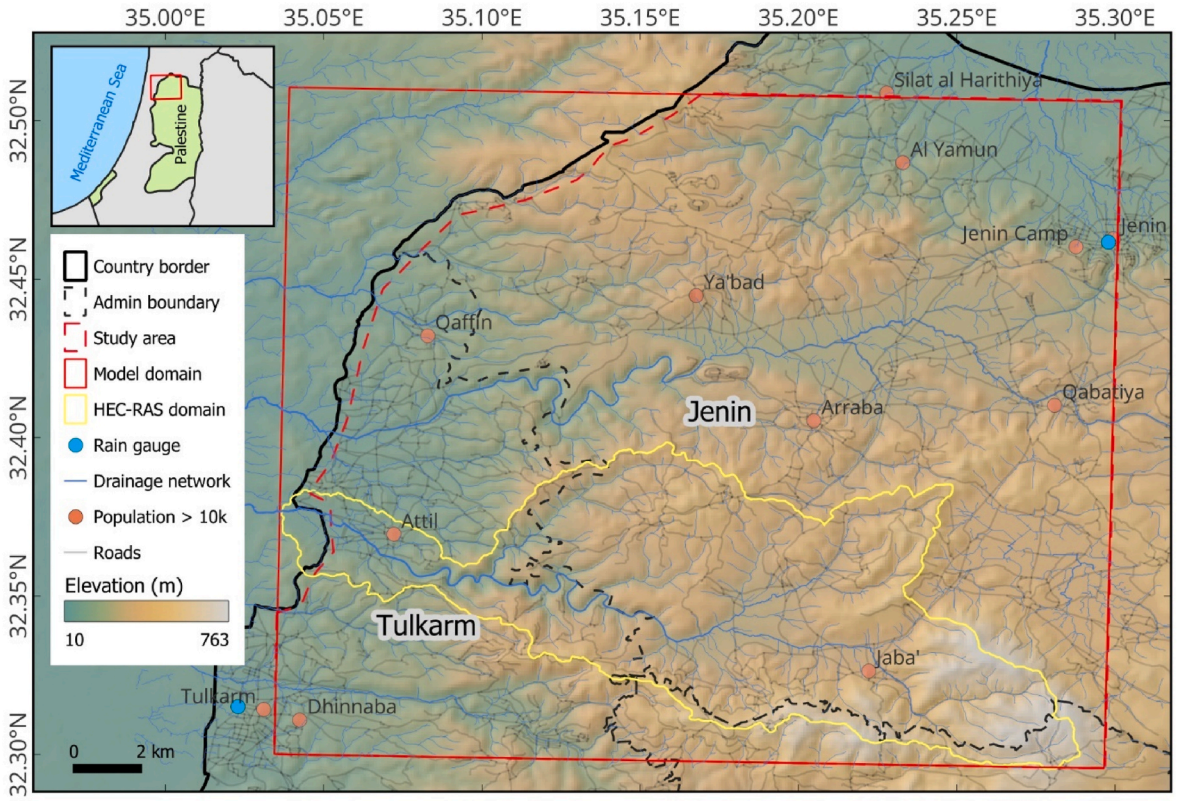

Fig. 1. Study area spanning the Jenin and Tulkarm administrative governorates in the West Bank, Palestine. Rain gauge stations in Jenin and Tulkarm are shown. The Nablus rain gauge station is 9 km to the south of the study area.

particularly damaging flood event followed heavy and sustained winter rainfall in early January 2013, which affected 12,500 people and caused widespread damage to agricultural land [44,45]. The flooding highlighted existing vulnerabilities and the importance of advancing disaster risk reduction strategies and community and government levels [45]. The main landcover classes in the study area are grassland (45 %), shrubland (17 %), tree cover (16 %), cropland (11 %) and built-up (10 %) (Table S1).

3. Methodology

3.1. Digital elevation model (DEM) preparation and analysis

A 10 m resolution DEM was created to underpin the flood hazard modelling. Contour lines at 1 m vertical intervals were supplied by the Ministry of Local Government (Palestine) covering the study area and the *Topo to Raster* tool in ArcGIS Pro 3.0 was used to interpolate a digital elevation model at 10 m resolution. This tool uses an iterative finite difference interpolation technique based on the ANUDEM program [46]. The method and date of acquisition of the contour lines were not known. Therefore, we compared a hillshade of the DEM to satellite imagery in Google Earth to estimate an acquisition date of 2015–2016, based on the construction date of large buildings that were apparent in the DEM. Differencing the 10 m custom DEM from the 30 m Copernicus Digital Elevation Model (GLO30) revealed spatially variable offsets and artefacts (Fig. 2a). Therefore, five components of the DEM were defined for independent adjustments to improve the DEM before flood hazard modelling ([1] to [5] shown in Fig. 2a). Component [1] extended the custom DEM beyond the study area to avoid boundary effects in the flood modelling and was filled with the GLO30 DEM. Components [2, 3 and 5] were coregistered to the GLO30 DEM independently to correct their systematic offsets using a blockwise coregistration pipeline in the xDEM Python package, which incorporated a bias correction, iterative closest point registration, followed by the coregistration of Nuth and Kääb [47]. Component [4] was replaced with the GLO30 DEM due to the presence of systematic artefacts. The refined custom DEM had a normalised median absolute deviation (NMAD) of 0.67 m when differenced with the GLO30 DEM, compared to 2.22 m before adjustment (Fig. 2). Components [1] and [4] were excluded from this NMAD calculation since these were areas filled with the GLO30 DEM. Hydrological conditioning was applied to the coregistered 10 m custom DEM using the *BreachDepressionsLeastCost* tool in Whitebox 1.4.0 [48] with a maximum breach distance of 1 km. A stream network was then derived using a flow accumulation threshold of 1000 cells, which was selected based on a visual inspection of stream sources using the Google Satellite Imagery basemap in QGIS.

3.2. Earth observation data

3.2.1. RapidEye imagery

Pre- and post-flood availability of RapidEye satellite imagery was used to assess the flood extent of the flooding in January 2013. Two multi-spectral 5 m resolution RapidEye-1 satellite images (December 31, 2012 and January 15, 2013) processed to surface

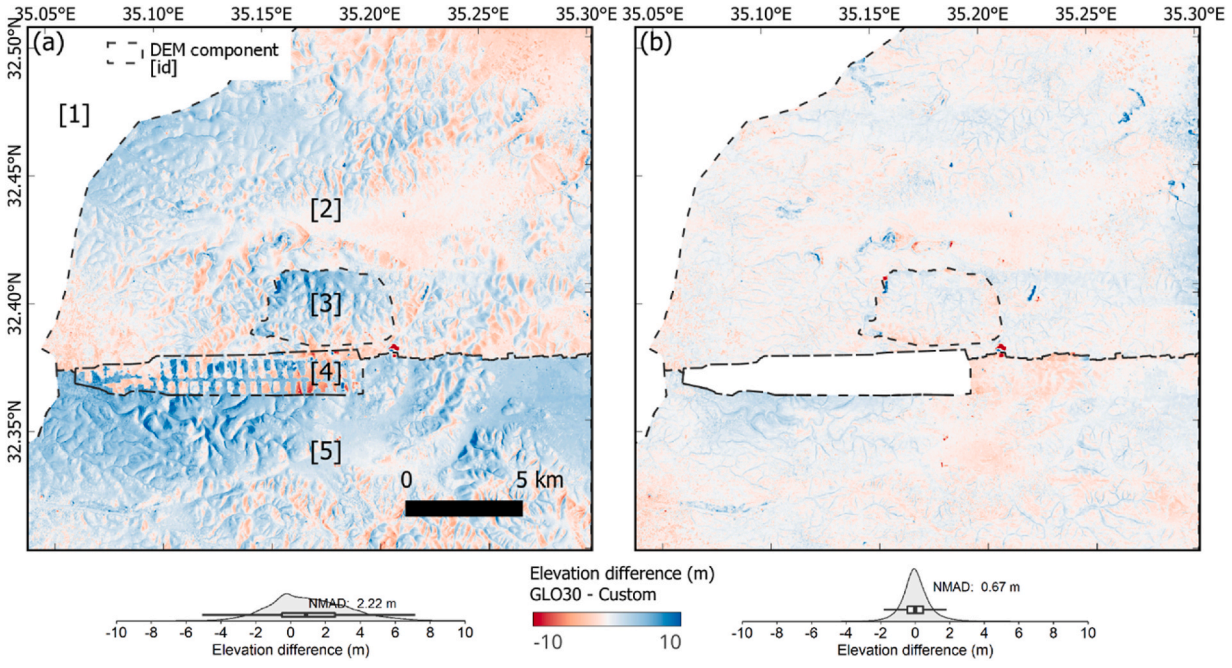

Fig. 2. (a) DEM of difference between the GLO30 DEM and the custom DEM derived in this study from contour data. Labelled components are discussed in the text. (b) DEM of difference post-coregistration to the GLO30 DEM.

reflectance (L3A) were accessed from PlanetLabs. The 2013 image was co-registered to the 2012 image using Cosi-Corr [49] and ENVI 5.6.3 to remove a spatially variable misregistration (east-west mean offset: 6.4 ± 6.3 m, north-south mean offset: 4.2 ± 6 m) using a second order polynomial. A normalised difference vegetation index (NDVI) (1) was derived for the two acquisitions using the near infrared and red bands.

$$NDVI = \frac{(Nir - Red)}{(Nir + Red)} \quad (1)$$

High chlorophyll reflectance in the Nir band compared to low reflectance in the red band means the NDVI is an indicator of vegetation presence and health [50,51]. The difference in NDVI values pre- and post-flood can be used to reconstruct the inundated extent using the change in reflectance of the damaged or scoured vegetation, which would be observed as an NDVI decrease [52,53]. The short timespan between the RapidEye acquisitions of our study side (15 days) meant that changes in NDVI values were expected to primarily correspond to the effects of the extreme rainfall and flooding on vegetation. To mask out insignificant change in NDVI, we manually digitised 'stable' sample polygons over areas where the spectral reflectance was less likely to be affected by the flooding, such as woodland and bare ground, and extracted their NDVI difference values pre- and post-flood. We then masked pixels with NDVI difference values less than two times the standard deviation of these stable polygons (NDVI<0.06) and sieved the output to retain connected clusters of at least 18 pixels (450 m^2). This mask is shown in Fig. S1. Finally, we intersected the remaining NDVI changes with the stream network derived in Section 3.1 to determine whether they were likely the consequence of fluvial flooding. The Shreve stream order [54] was allocated to the stream network derived in (3.1) and these values were used to sample the NDVI difference to investigate the relationship between stream order and the pre- and post-flood magnitude of NDVI change.

3.2.2. Land cover

ESA WorldCover 10 m v200 dated 2021 [55] was used to quantify the landcover of each area of significant NDVI change (3.2.1). We quantified this for both the full study area (506.5 km^2)(Fig. 1), which included NDVI changes corresponding to pluvial and fluvial flooding and agricultural activity, and separately for the NDVI changes directly connected to the stream network (Fig. 1), which were most likely to be caused by fluvial flooding. The 10 m pixel size of the ESA WorldCover land cover map would in some cases incorporate mixed pixels of urban structures, roads, tracks, and vegetation for example, given that these features are generally small within the study area. Therefore, to evaluate potential inundation impacts for urban areas, we also used building footprints from the Global ML Buildings dataset [56], and the transportation network including roads and tracks from OCHA [57], which were more complete than OpenStreetMap data.

3.3. Rainfall data and climate scenarios

Daily rainfall data for the January 2013 flood event were available from the Palestine Meteorological Department for Jenin (JEN00001, 145 m elevation), Tulkarm (TUL00002, 7 m elevation), and Nablus (NAB00003, 73 m elevation) stations (Figs. 1 and 3a).

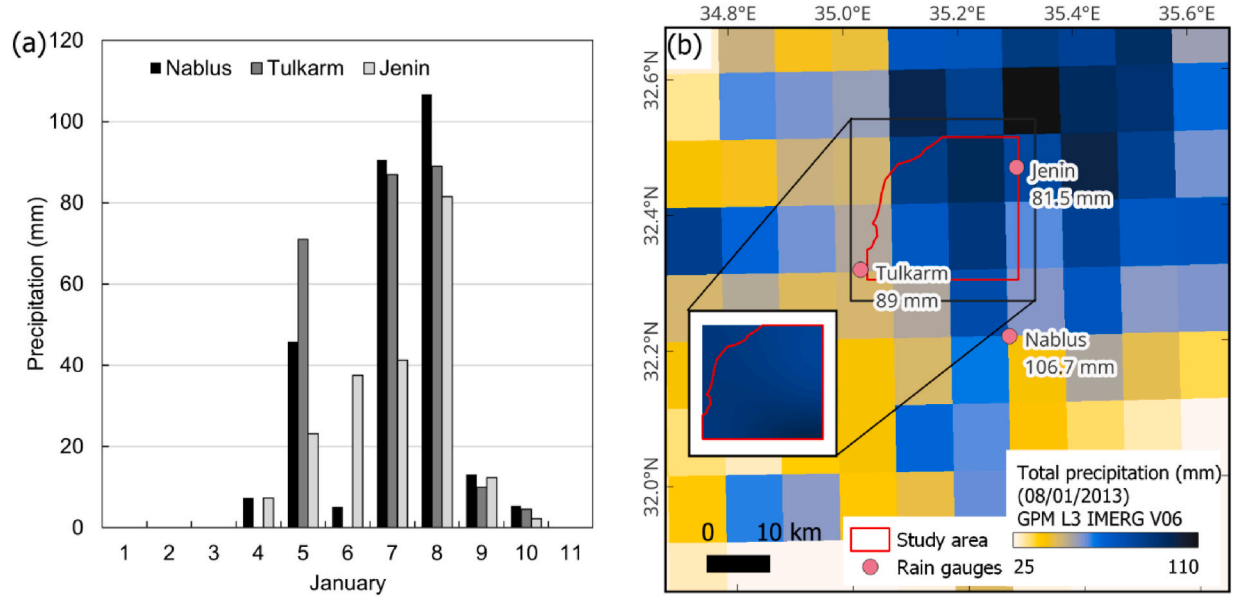

Fig. 3. Rainfall data for the January 2013 flood event. (a) Rainfall recorded at three rain gauges bounding the study area. (b) Rainfall derived from the GPM L3 IMERG V06 product on the January 8, 2013 and interpolated rainfall between the three rain gauges for the study area (inset). Labelled values correspond to the total recorded rainfall on January 8, 2013.

Inverse distance weighted interpolation was used to create a grid representing peak rainfall (mm/hour) from the station data on 8th January (Fig. 3b). We also downloaded the total rainfall on the January 8, 2013 from the calibrated GPM L3 IMERG V06 precipitation product [58] for comparison with the gauge stations (Fig. 3b).

Historical and future projected rainfall data were used in a climate change analysis. Historical rainfall data recorded at Nablus station (NAB00003) (9 km south of the study area) from 1985 to 2014 were provided by the Palestine Meteorological Department. Coupled Model Intercomparison Project Phase 6 (CMIP6) Global Circulation Models (GCMs) are used for the future projected rainfall data. The GCMs selected for this study are GFDL-ESM4 and MPI-ESM1-2-HR, as evaluated by Hamed et al. [59] and Mesgari et al. [60]. However, we acknowledge that using only two models introduces additional uncertainties into the climate change projections. Hamed et al. [59] compared CMIP5 and CMIP6 models over the Middle East and North African (MENA) region using historical simulations and future projections, while Mesgari et al. [60] provides an assessment of CMIP6 models' performances and projection of rainfall based on Shared Socio-economic Pathways (SSPs) scenarios over Middle East, North Africa, Afghanistan, and Pakistan (MENAP). The two SSPs considered in this study are SSP2-4.5 (medium challenges to mitigation and adaptation), and SSP5-8.5 (high challenges to mitigation, low challenges to adaptation). The time period of 1985–2014 is considered as historical. The time periods of 2021–2040, 2041–2060 and 2081–2100 are classified as near future, mid-future, and far future respectively, in accordance with IPCC AR6.

We analysed the historical rainfall patterns and characteristics, with focus on RX1day (annual maximum 1-day rainfall) (e.g. Ref. [17]). It was not possible to determine the precise duration of the rainfall causing the 2013 flooding, but we not that for the station in the upper catchment (Jenin), the majority of rainfall fell on the 8th January (Fig. 3a). However, we acknowledge that RX1day does not capture multi-day extremes or the cumulative precipitation that can influence flood magnitude. First, the GCM data were bias corrected and statistically downscaled to the desired spatial and temporal resolution. The bias correction and statistical downscaling were undertaken using the empirical quantile mapping method, which maps the probability distribution of rainfall of GCMs with the probability distribution of the observed rainfall. The concept of quantile mapping can be understood as:

$$X^{corr}_{future,t} = inverse\ ecdf\ ^{obs}_{reference}\left(ecdf^{Model}_{reference}\left(X^{Model}_{future,t}\right)\right) \quad (1)$$

Here, *ecdf* is the empirical cumulative distribution function for the reference time period, $X^{Model}_{future,t}$ is the raw GCM at time t in the future, $ecdf^{Model}_{reference}$ is the empirical cumulative distribution function of the GCM for the reference period, $inverse\ ecdf\ ^{obs}_{reference}$ is the inverse empirical cumulative distribution function of the observed rainfall for the reference period, and $X^{corr}_{future,t}$ is the corrected estimate of $X^{RModel}_{future,t}$. The monthly *ecdf* for this study was developed using the observed rainfall data at Nablus station and GCM hindcast data for the period 1985–2014. Gudmundsson et al. [61] illustrates this procedure in detail. Stationary or non-stationary rainfall frequency analysis was then performed on the bias corrected RX1day values based on the Mann Kendall trend test, to quantify the rainfall value associated with a given return period [62,63]. The temporal disaggregation of rainfall values from the rainfall frequency analysis was done using the Global Precipitation Measurement (GPM) - Integrated Multi-satellitE Retrievals for GPM (IMERG) (GPM-IMERG) of half hourly temporal resolution and $0.1^\circ \times 0.1^\circ$ spatial resolution based on the highest flood event recorded in Nablus.

3.4. Flood modelling

3.4.1. January 2013 flooding

Three models were used to simulate the January 2013 flooding and evaluate their performance speed and accuracy: FastFlood v0.12 (website tool version) is a new computationally efficient model that has shown good agreement with fully dynamic physics-based models whilst requiring up to 1500 times less computation time [64]; HAIL-CAESAR is a high performance version of the Caesar-Lisflood model that uses simplified shallow-water equations [65]; and HEC-RAS 6.4.1 is a physics-based hydraulic model capable of 2D unsteady flow simulations using Shallow Water Equations. The data input and parameters for the flood models are shown in Table 1. In the absence of validation data in our catchment, we used standard model parameters and performed sensitivity testing to Manning's roughness values, which were uniformly applied across the study area for each simulation. Spatially variable roughness values are preferable to capture detailed inundation characteristics, for example informed by a landcover map. However, applying a uniform value is common where landcover data are not sufficiently high resolution or are uncertain, and where there is a lack of field-base information to inform spatially variable Manning's values [17,66–68]. Model sensitivity to the roughness value was determined by increasing the value from 0.01 to 0.07 in 0.01 increments and assessing the modelled flood extent for depths greater than 0.1 m against the NDVI-derived reference data (Section 3.4.2). The FastFlood and Hail-Caesar models were run for the model domain shown in Fig. 1 and the outputs were then clipped to the study area to avoid artefacts at the model boundary. A smaller study catchment was used for the HEC-RAS simulations to make them computationally viable, which was subsequently used as the reference area to compare the outputs from all three flood models.

3.4.2. Model comparison

Modelled flood depth was evaluated against the NDVI changes that intersected with the stream network, which indicated the removal or damage of vegetation during the 2013 flood (Section 3.2.1). FastFlood and HAIL-CAESAR were run across the full study area (Fig. 1), whereas HEC-RAS was run for a smaller catchment due to computational limitations. Therefore, the models were evaluated across these two domains. Since the NDVI changes were not expected to be fully representative of the observed flood extent, for example on banks lacking vegetation, polygons of NDVI decrease that intersected with the stream network and that visually appeared to correspond to the 2013 flood event (Section 3.2.1) were manually selected. These polygons were manually edited in some

Table 1
Flood model input parameters.

Model	DEM	Rainfall data	Settings	Manning's Roughness values tested
FastFlood	10 m resolution (Section 3.1) clipped to the study area (Fig. 1)	January 8, 2013 interpolated grid (mm/hr) (Section 3.3, Fig. 4b)	Solver: very high quality	0.01–0.05
HAIL-CAESAR		January 8, 2013 hydro index of three rainfall zones (mm/hr) for 24 h	See the example parameter file in the supplement	0.01–0.05
HEC-RAS	10 m resolution (Section 3.1) clipped to HEC-RAS domain (Fig. 1)	January 8, 2013 interpolated grid (Section 3.3, Fig. 4b) (mm/hr) for 24 h	Downstream boundary: normal depth Computation interval: 10 s Equations: SWE-ELM	0.01–0.07

cases to improve their representation of the inundation extent (e.g. Fig. S2b). Buffers of 110 m were then created from both sides of the stream centreline and these were clipped to encompass the NDVI polygons to form validation areas (Fig. S2). These areas were then used to derive accuracy assessment scores for each flood model. The F1 score (2), which is a weighted average of precision (ratio of the true positive modelled flood area to the total modelled flood area) and recall (ratio of true positive modelled flood area to the total reference (NDVI) flood area), was used to represent overall model accuracy on a 0–1 scale where 1 is the highest accuracy [69,70]. Additionally, the intersection over union (IoU) ratio (3) was used to quantify the amount of overlap between the predicted flood extent and the NDVI reference extent.

$$F1\ score = \frac{(\text{Precision} \times \text{Recall})}{(\text{Precision} + \text{Recall})/2} \tag{2}$$

$$\text{IoU} = \frac{\begin{pmatrix}\text{Intersecting area of the predicted flood extent}\\ \text{and the reference flood extent}\end{pmatrix}}{\begin{pmatrix}\text{Combined area of prediced flood extent}\\ \text{and the reference flood extent}\end{pmatrix}} \tag{3}$$

4. Results

4.1. January 2013 flooding

Peak rainfall during the 2013 flooding occurred on the 8th of January with 106.7, 89.0, and 81.5 mm of rainfall recorded at Nablus, Tulkarm, and Jenin rain gauges respectively (Fig. 3). The GPM L3 IMERG V06 satellite product showed a maximum of 96.1 mm total rainfall in the study area for the same day, which was observed closest to Jenin station (Fig. 3b).

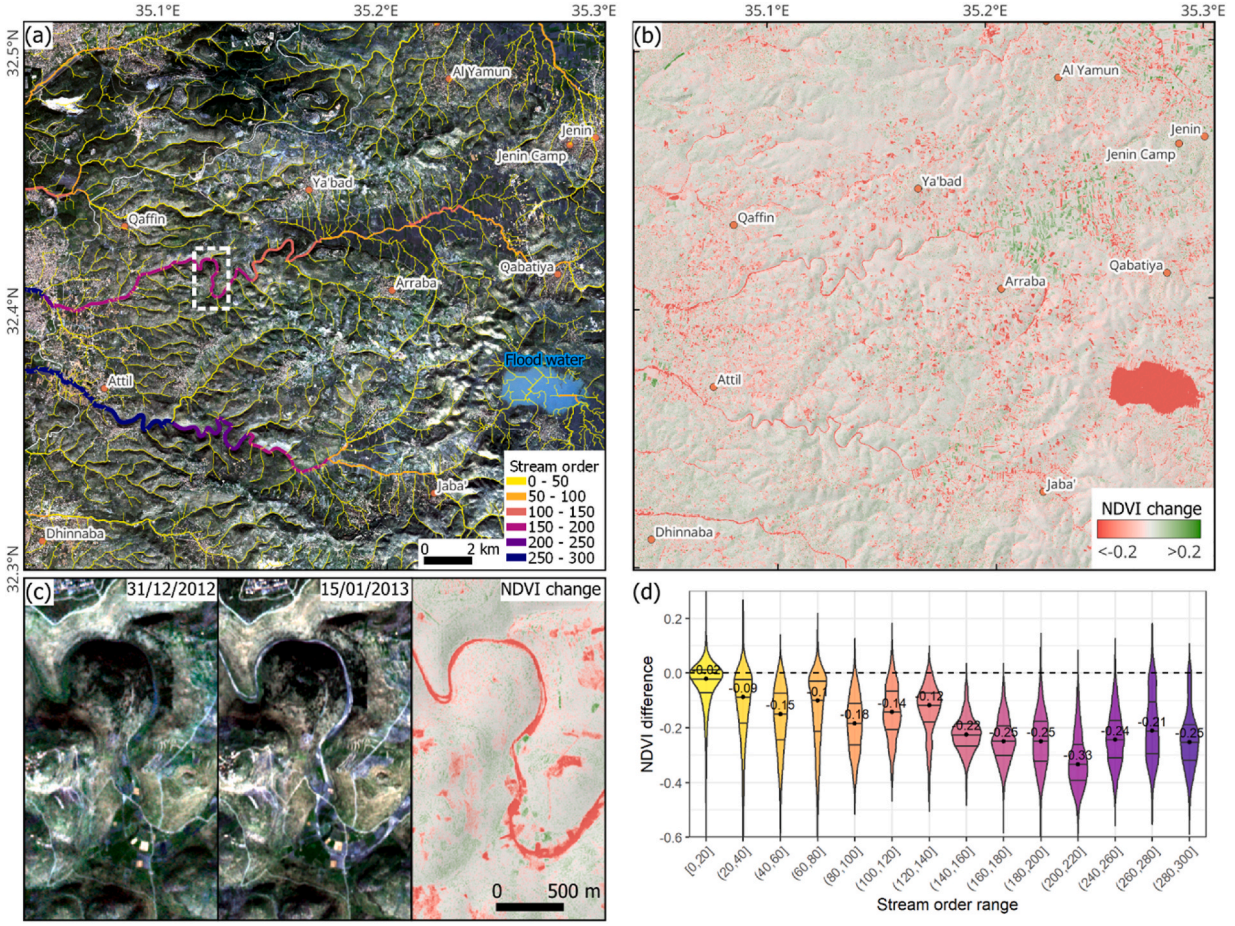

Fig. 4. (a) Shreve stream order in the study area. (b) NDVI change derived from pre- and post-flood RapidEye imagery. (c) Example of the pre- and post-flood RapidEye imagery with the corresponding NDVI change. (d) NDVI difference plotted with increasing stream order. Basemap (a and c) is a RapidEye-1 image (January 15, 2013). Image © 2013 Planet Labs PBC.

4.1.1. NDVI change

The effects of the January 2013 flood event were evident in decreased NDVI values across the study area, particularly corresponding to the stream network and a large area of ponded water that accumulated during the storm (Fig. 4). NDVI changes were not exclusively confined to the stream network and incorporated the effects of pluvial flooding and seasonal agricultural activity. The RapidEye images spanned a fifteen-day window, and the post-flood image was captured five days after the peak rainfall, therefore the effects of vegetation change unrelated to the storm event were minimised. However, NDVI increases northeast of Arraba town were related to specific agricultural activities (Fig. 4b). It was noted from Sentinel-2 data that NDVI values are typically increasing across the study area between the months of December–January and that this is also a time of crop harvest (Fig. S3). There was a clear non-linear relationship between NDVI decrease and increasing Shreve stream order (Fig. 4d). Except for stream orders 0–20, the median NDVI decrease for other streams exceeded the expected uncertainty of 0.06, with stream orders 200–220 displaying the largest median NDVI decrease of −0.33 (Section 3.2.1). The highest stream orders displayed greater spread in the NDVI change (Fig. 4d), likely due to a combination of their less ephemeral nature, greater carrying capacity, and lower detection of NDVI changes for channels in built-up environments due to sparser vegetation coverage. Therefore, using NDVI change to derive reference flood extents would not be appropriate in urban areas; However, the deposition of sediment in these areas could be used instead if they had sufficient spectral contrast to the surrounding roads and buildings [71].

The total area of NDVI decrease and increase across the study area was 65.3 km^2 (12.9 % of the study area) and 12.4 km^2 (2.5 % of the study area) respectively (Fig. 5a), with the cropland land cover class displaying the greatest extent of NDVI decrease and NDVI increase with 13.2 km^2 (24 % of all cropland) and 6.1 km^2 (11 % of all cropland) of land affected respectively. One limitation is that these statistics were derived from the closest in time high-resolution land cover map (2021), so are not fully representative of the landcover at the time of flood. The NDVI decrease intersecting with the stream network, which was most likely to be a direct result of the effect of moving water on the vegetation, totalled 35.1 km^2 (6.9 % of the study area) and cropland was the class most affected (10.5 km^2, 19 % of all cropland) followed by grassland (9.4 km^2, 4.1 % of all grassland) (Fig. 5b). The area of NDVI decrease also included 1.8 km^2 (3.5 %) of the built-up area (Fig. 5b). Non-fluvial NDVI change represents a vegetation response to the storm precipitation or standing water, although these areas may still drain into lower order streams. Here, NDVI decrease was greatest for grassland (12.6 km^2, 5.5 % of all grassland) (Fig. 5c).

4.1.2. Flood model comparison

The modelled inundation extent across the full study area was 21.84 km^2 for FastFlood and 17.42 km^2 for HAIL-CAESAR for the 2013 flood event (Table 2). For the smaller HEC-RAS domain, the inundated areas were 3.05 km^2, 2.99 km^2, and 4.80 km^2 for FastFlood, HAIL-CAESAR, and HEC-RAS respectively (Table 2). FastFlood and HAIL-CAESAR were compared across the full study area,

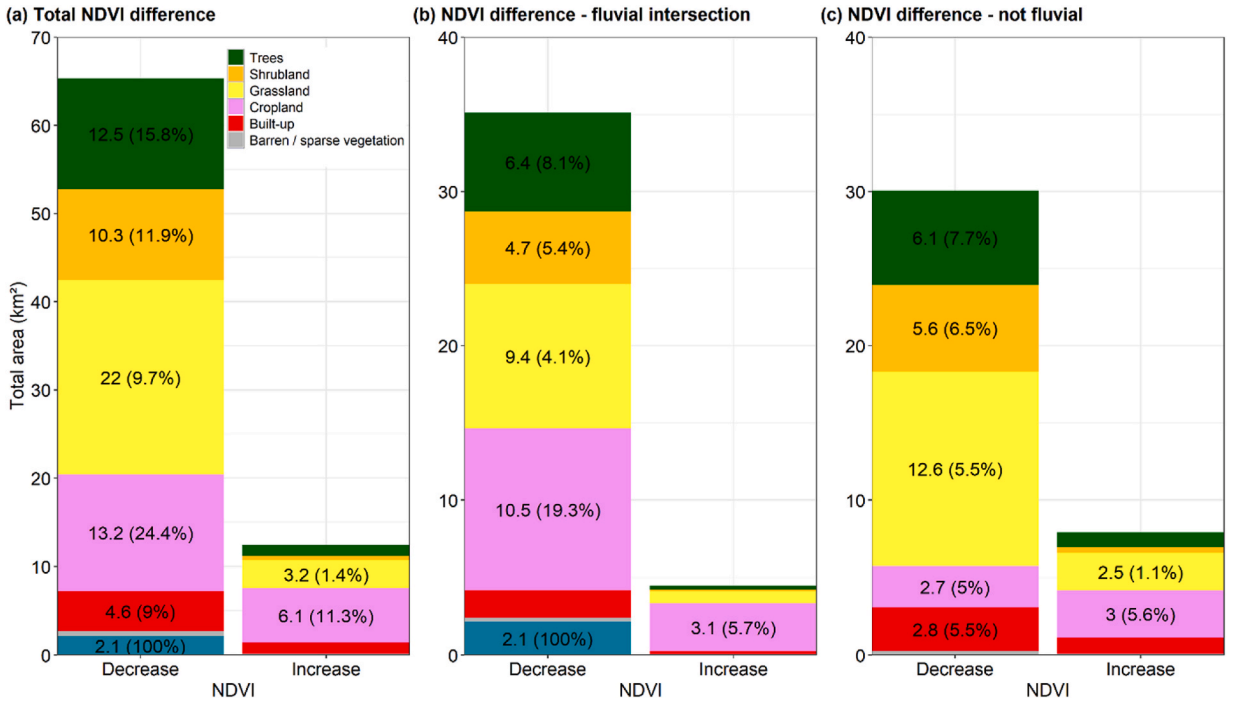

Fig. 5. (a) NDVI increase and decrease in the study area coloured by the corresponding land cover extracted from ESA World Cover v200. (b) NDVI increase and decreases for areas connected to the stream network and (c) for areas not connected to the stream network. The area of each class in square kilometres is labelled. Percentages represent the class area as a percentage of the total area of each land cover class in the study area. Bars are coloured by their land cover class.

and all three models were directly compared in the HEC-RAS study domain (Table 2). Here, the F1 accuracy scores were 0.74, 0.75, and 0.76 for FastFlood, HAIL-CAESAR, and HEC-RAS respectively (Table 2). Similarly, the HEC-RAS model displayed the highest IoU score (0.61), although FastFlood (0.59) and HAIL-CAESAR (0.60) were similar (Table 2). The Manning's *n* values used in these models were 0.03, 0.02, and 0.06 respectively and the sensitivity of model accuracy to Manning's *n* values was low in the tested range of 0.01–0.06 (Table S2). The modelled flood depths from HAIL-CAESAR were a closer match to HEC-RAS compared to FastFlood (Fig. 6). Here, FastFlood depths had a mean difference of −0.03 m and a mean absolute error of 0.51 m when compared to HEC-RAS, compared to 0.21m and 0.36 m respectively for HAIL-CAESAR (Fig. 7).

4.2. Future climate and flood hazard

4.2.1. Climate

Biases in the long term mean monthly rainfall between observed rainfall at Nablus rain gauge and the selected GCMs (Fig. 8a) were observed. Although the GCMs were able to capture the monthly rainfall pattern, significant biases were observed between the observed and modelled datasets. Fig. 8b shows the historical RX1day with future bias corrected RX1day for the two climate models and SSP scenarios we tested. A maximum increase of 18 % and 24 % with respect to the historical RX1day was seen in GFDL-ESM4 and MPI-ESM1-2-HR, respectively, for the SSP2-4.5 near future period (2021–2040) (Table 3). A negative change in RX1day, contrary to the majority of other locations worldwide [72], was observed in SSP5-8.5 scenario in the mid-future, whereas no changes in RX1day can be observed in SSP5-8.5 scenario in the near future period.

The Mann-Kendall trend test performed on bias-corrected future RX1day values indicated no significant trends, prompting the application of stationary rainfall frequency analysis using Gumbel's method. Table 4 shows the changes in RX1day with respect to historical data for different return periods in the mid-future period, for both GCMs and both SSPs. For both the scenarios, GFDL-ESM4 projected a decrease in RX1day, whereas MPI-ESM1-2-HR projected an increase as high as 39 %. This difference highlights the uncertainties inherent in climate models and future climate for the region. The return period rainfall for the near future, mid-future, and far future is shown in Fig. 9. Both models showed an increase in rainfall compared to historical RX1day, except for GFDL-ESM4 in the mid-future (Fig. 9b). Higher changes were observed in SSP5-8.5 for the near future, while SSP2-4.5 showed more significant changes in the far future.

4.2.2. Flood hazard

The rainfall recorded on the January 8, 2013 (106.7, 89.0, and 81.5 mm of rainfall for Nablus, Tulkarm, and Jenin rain gauges respectively) corresponded to a historical return period of between 1 in 5 (89 mm) to 1 in 10 years (103 mm) (Table 4). A 1 in 100-year event based on historical data (1985–2014) would feature 148 mm of rainfall. The highest projected future rainfall for a 1 in 100-year event (205 mm) was estimated by the mid-future (2041–2060) MPI-ESM1-2-HR model and SSP2-4.5 scenario (Table 4). Owing to the uncertainty in the future climate between the GFDL-ESM4 and MPI-ESM1-2-HR models (Table 4), we modelled both these rainfall events to quantify the impacts of higher magnitude flooding. To derive a spatially variable rainfall grid, the Nablus rainfall scenarios were scaled proportionally for Tulkarm and Jenin stations using the 2013 flood rainfall distributions (Table 5). Only FastFlood and HAIL-CAESAR were applied across the study area due to the computational limitations of using HEC-RAS over the large domain.

FastFlood produced the largest inundated area for each 1 in 100-year rainfall scenario, with 26.84 km^2 inundated for the future 1 in 100-year rainfall event (Table 5). This model also inundated the greatest length of transportation network including roads and track (111.5 km or 9.2 % of the total length in the study area), and the largest area of cropland (14.5 km^2 or 25.3 % of all cropland in the study area) (Fig. 10d). However, the HAIL-CAESAR model for the same scenario inundated a larger number of buildings (n = 3207) (Fig. 10c). Differences in the modelled inundation between FastFlood and HAIL-CAESAR were apparent in the low relief area north of Arraba town where FastFlood produced greater floodplain inundation (Fig. 10).

5. Discussion

Strategies to reduce flood risk are becoming more urgent as the probability of extreme rainfall events increases with climate warming [1,2]. In lower income countries, this is coupled with unregulated development into hazardous areas, undeveloped infrastructure to manage flood waters, and a lack of flood hazard maps required for decision making [24,41,43,73]. Reliable urban flood hazard modelling requires accurate and typically high resolution (<10 m) DEMs, combined with past flood inundation data, both of

Table 2
Flood model accuracy assessment for the 2013 flood compared to the NDVI-derived inundation extents.

Extent	Model	Mannings	F1 score	Precision	Recall	IoU	Inundated area (km^b)	Model runtime
Study area	FastFlood	0.02	0.72	0.70	0.73	0.56	21.84	~40 s[a]
	HAIL-CAESAR	0.03	0.73	0.75	0.71	0.57	17.42	~7 h[b]
HEC-RAS domain	FastFlood	0.03	0.74	0.73	0.76	0.59	3.05	Clipped from full study extent
	HAIL-CAESAR	0.02	0.75	0.75	0.75	0.60	2.99	
	HEC-RAS	0.06	0.76	0.68	0.86	0.61	4.80	~4 h[a]

[a] Desktop PC with 14 cores (3.3 Ghz).
[b] High Performance Computing node with 40 cores (2.0 Ghz).

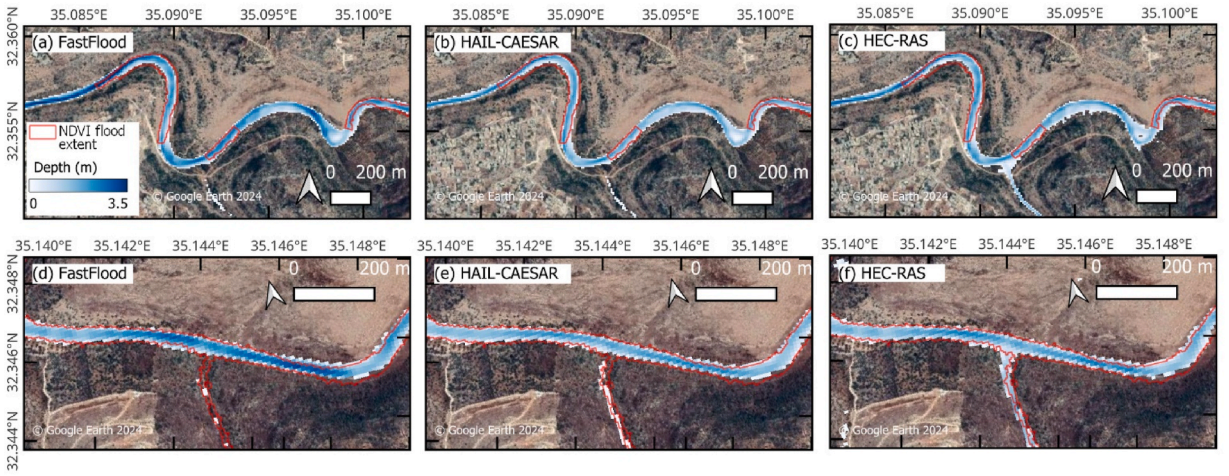

Fig. 6. Example modelled flood depths for the January 2013 rainfall event at two locations. NDVI-derived validation extents are shown as red polygons.

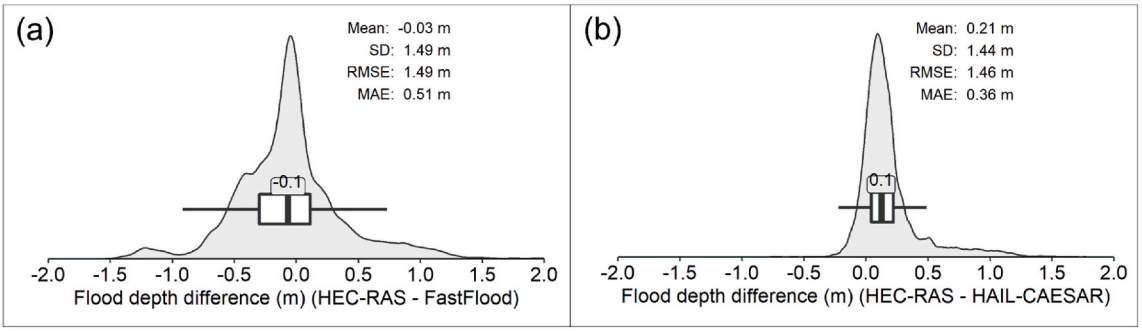

Fig. 7. Flood depth difference boxplots (median value is labelled) and half violin plots. (a) HEC-RAS flood depth minus FastFlood. (b) HEC-RAS flood depth minus HAIL-CAESAR. Mean, standard deviation (SD), root mean square error (RMSE), and mean absolute error (MAE) are shown.

which are not globally available or open access [17,18,67,74]. Therefore, site-specific approaches are often required. In this study, we used flood extents observed in satellite imagery to evaluate three flood models, which were underpinned by a bespoke 10 m resolution DEM and future climate projections incorporating local rain gauge observations (1985–2014).

Satellite imagery spanning the January 2013 flood event was used to derive NDVI's that captured damaged and scoured vegetation reflecting the flood extent (Fig. 4). Similar approaches have been used elsewhere to observe flash flood inundation extents [52,53]. However, this method does not represent a definitive flood map since not all riparian areas will experience vegetation loss or damage, and seasonal agricultural activity including crop harvest could bias the observations, as was indicated in our study. Where available, shorter time separations between the flood event and satellite data would help minimise this, but the shortest in this case was a fifteen-day separation. Nonetheless, NDVI difference maps (Fig. 4) revealed widespread flood impacts to cropland (24 % of cropland in the study area) (Fig. 5), which supports observations of widespread damage to crops in the northern West Bank reported by OCHA [45] and contrasts with the typical increase in NDVI at the time of year of the flood (December–January) (Fig. S2). Additionally, the 2013 flooding prompted the formation of the Palestinian Agricultural Disaster Risk Reduction and Insurance Fund (PADRRIF) to reduce agricultural damage and losses [75]. Probabilistic flood hazard mapping is a key mechanism to enable this preparatory risk mitigation and preparedness.

In the absence of gauging station data or other flood extent observations, NDVI differencing provided the basis to evaluate three flood models' ability to simulate the 2013 event (Table 2 and Fig. 6). As expected, the physics-based flood models HEC-RAS and HAIL-CAESAR best matched the NDVI-derived flood extent, followed by FastFlood (Table 2). Similar accuracy assessment F1 scores of 0.74, 0.75, and 0.76 for FastFlood, HAIL-CAESAR, and HEC-RAS respectively showed that all models provided a reasonable match to the NDVI-derived flood extent. Additionally, FastFlood's run time of 40 s for the full study area without requiring high-performance computing or complex model setup, demonstrates its value in providing useful flood hazard information, particularly where numerical modelling resources are limited [20,64,76]. In this study we focused on the maximum flood extent and depths as an indicator of impact. However, we recognise that we could only validate flood extent due to the absence of flood depth information and gauging station validation data for the 2013 event. We were only able to validate the models against flood extents derived outside urban areas,

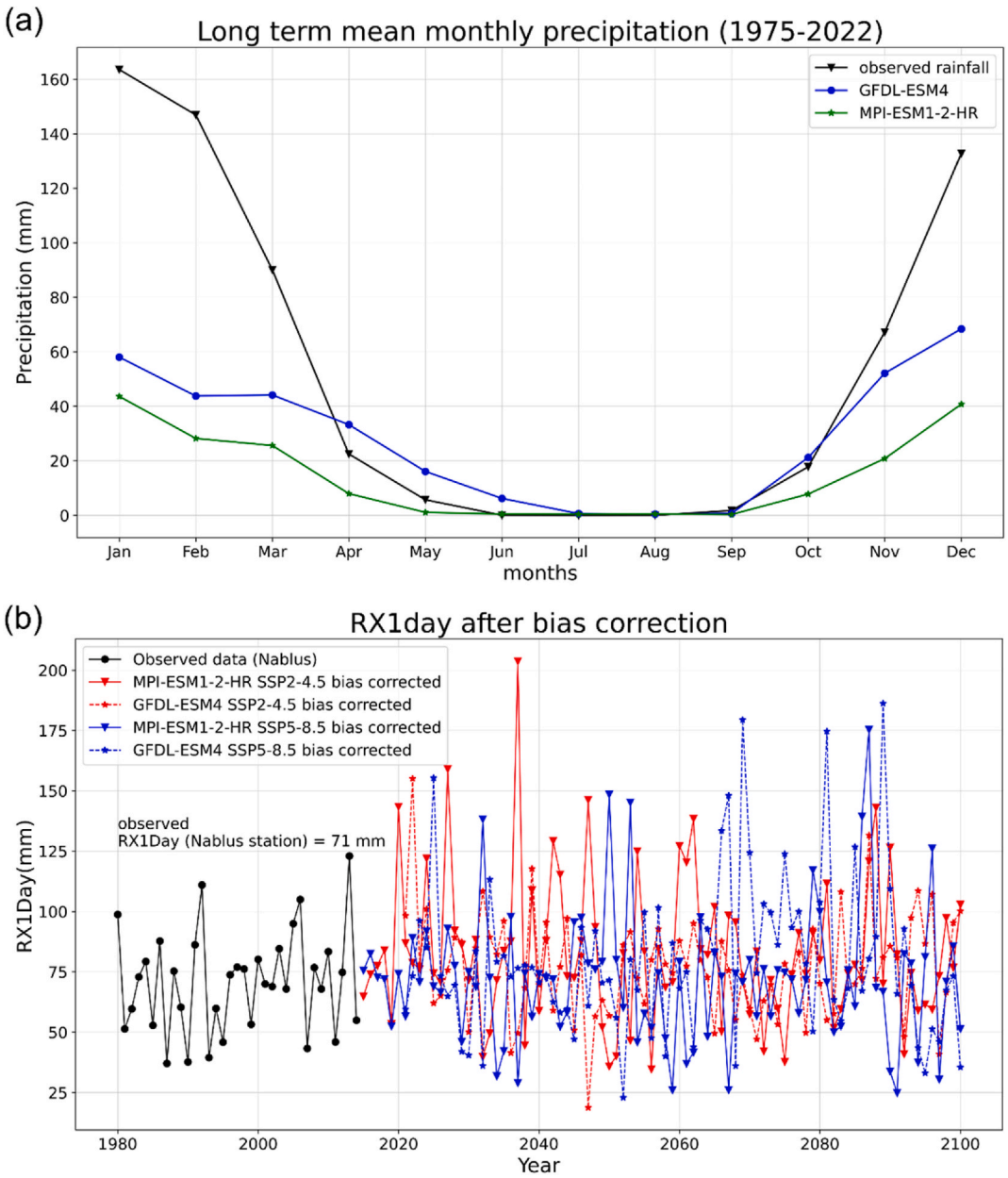

Fig. 8. Rainfall data analysis. (a) Long term mean monthly rainfall of GFDL-ESM4 and MPI-ESM1-2-HR, compared with observed rainfall. (b) Historical RX1day and future RX1day (after bias correction).

Table 3
Percentage changes in future RX1day after bias correction.

RX1day (mm) and % changes: GFDL-ESM4							
Scenarios	Historical 1985–2014	Near future 2021–2040	% change	Mid-future 2041–2060	% change	Far future 2081–2100	% change
SSP2-4.5	71	84	18	72	1	82	15
SSP5-8.5		76	8	68	−4	80	13
RX1day (mm) and % changes: MPI-ESM1-2-HR							
SSP2-4.5	71	88	24	83	17	82	15
SSP5-8.5		71	0	75	6	73	3

Table 4
Return period rainfall for GFDL-ESM4 and MPI-ESM1-2-HR, SSP2-4.5 and SSP5-8.5 for the mid-future.

Rainfall in mid-future (2041–2060) for SSP2-4.5					
Return Period (years)	Historical 1985–2014 (mm)	GFDL-ESM4 (mm)	% change	MPI-ESM1-2-HR (mm)	% change
5	89	89	0.2	112	26
10	103	102	−0.9	135	30
25	121	119	−1.9	163	34
50	135	132	−2.5	184	37
100	148	144	−2.9	205	39
Rainfall in mid-future (2041–2060) for SSP5-8.5					
5	89	86	−2.9	102	15
10	103	100	−2.8	123	19
25	121	118	−2.6	149	23
50	135	131	−2.5	168	25
100	148	145	−2.4	188	27

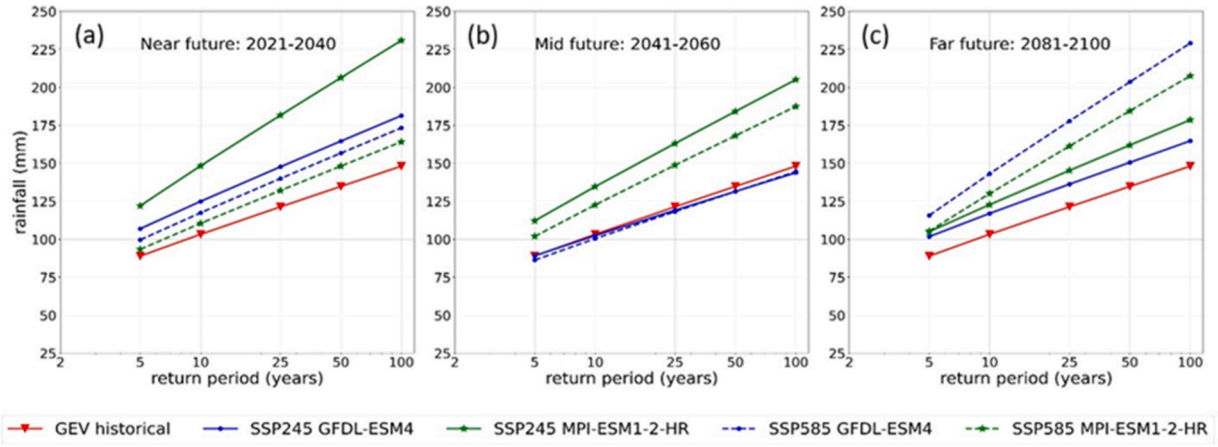

Fig. 9. Projected rainfall values for return periods and SSP2-4.5 and SSP5-8.5 for the near future (a), mid-future (b), and far future (c).

Table 5
RX1day rainfall scenarios and flood hazard.

Event	Nablus rainfall (mm)	Tulkarm rainfall (mm)	Jenin rainfall (mm)	Inundated area (km^2)
2013 flood	106.7	89.0	81.5	21.84 (FastFlood) 17.39 (HAIL-CAESAR)
Historical 1 in 100-year	148	123.4[a]	113.0[a]	23.17 (FastFlood) 17.94 (HAIL-CAESAR)
1 in 100-year mid-future (MPI-ESM1-2-HR model, SSP2-4.5 scenario)	205	171.0[a]	156.6[a]	26.84 (FastFlood) 21.41 (HAIL-CAESAR)

[a] Rainfall values were derived as a proportion of Nablus's rainfall according to the 2013 rainfall event.

where the spectral change in vegetation post-flood was clear. Within built-up areas, the deposition of sediment could be used to derive information on flood extent if it had sufficient contrast with the adjacent landcovers [71]. The lack of apparent deposition and supporting field observations, precluded this in our study. Additionally, dynamic flood effects, including arrival time, flow velocity, and depth, could also be better represented by physics-based flood models if gauging station validation data were available. These factors are key to more accurately assessing potential damages to agricultural land and buildings for example [77,78].

In studying the impacts of climate change, GCM projections are a primary source of uncertainty [79], which affects the successive steps including bias correction and rainfall frequency analysis [17]. Selecting models that accurately represent regional-scale climate is crucial for reducing uncertainty in future climate projections [80]. This study used GCMs recommended by Hamed et al. [59] and Mesgari et al. [60], which evaluated 11 climate models (CMIP5 and CMIP6 versions) over the MENA region and assessed the

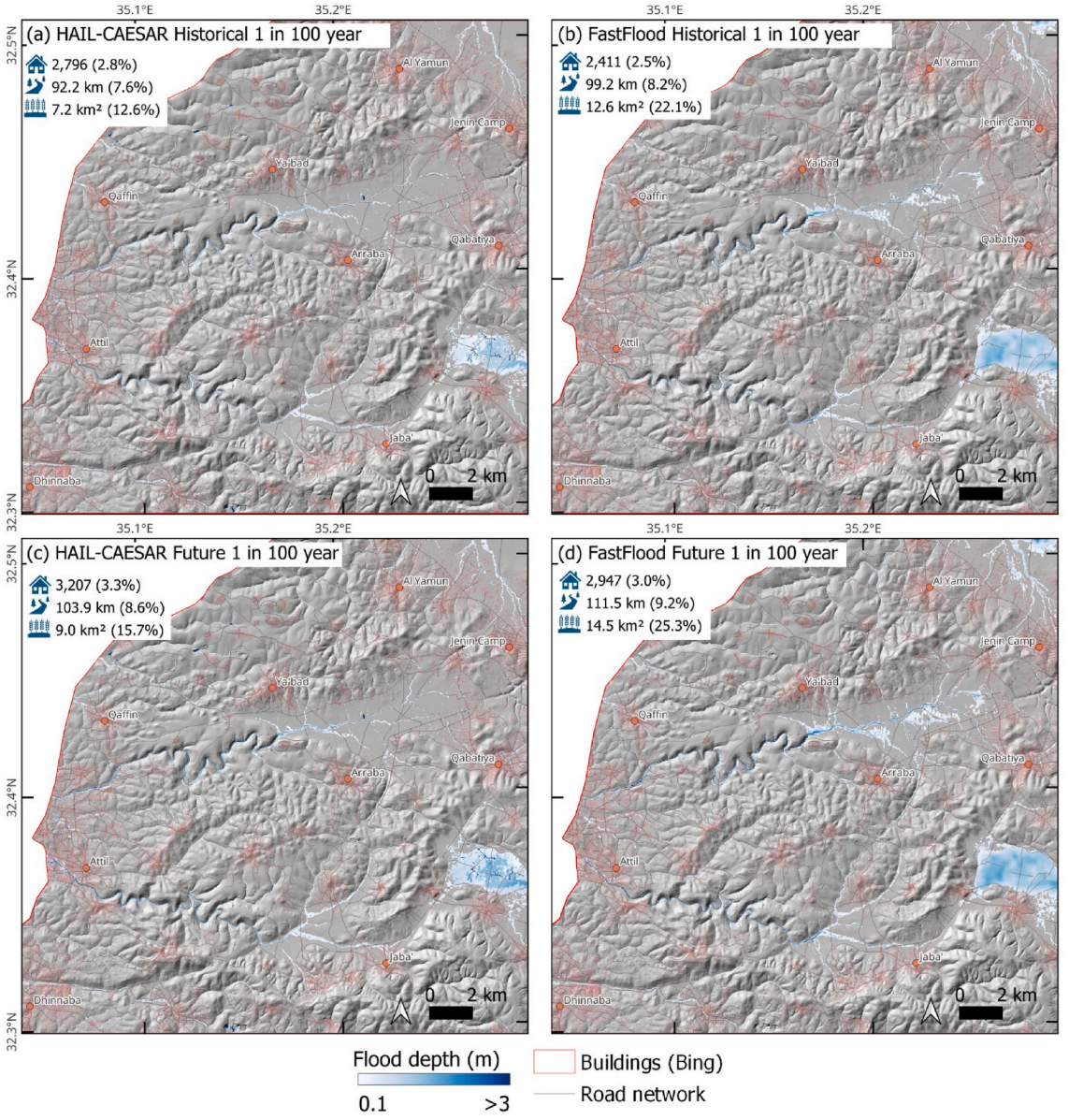

Fig. 10. HAIL-CAESAR and FastFlood flood inundation for historical and future (MPI-ESM1-2-HR model, SSP2-4.5 scenario) 1 in 100-year RX1day rainfall events. Impacts are shown for the number of buildings intersecting with the inundated area, the length of transport network within the inundated area, and the area of cropland within the inundated area. Percentages are with respect to the total number, length, or area of the features for the study area. Building footprints are from Microsoft [56], the road network is from OCHA [57], and the cropland area is from ESA WorldCover V200 [55].

performance of 11 CMIP6 models over the MENAP region, respectively. The inter-model variation can be seen in the return period rainfall values (Table 4). GFDL-ESM4 projects mainly negative precipitation changes with respect to historical values, while MPI-ESM1-2-HR projects increases of up to 39 %. Using an ensemble of GCMs, and models representative of Palestine's weather patterns could help reduce uncertainties in the climate change projections. For example, the flood hazard modelling study of Shrestha et al. [17] applied climate models representative of Nepal (warm-dry, cold-dry, warm-wet and cold-wet conditions), determined using the envelope-based approach by Lutz et al. [81]. Similarly, Richardson [82] followed a process-based evaluation based on McSweeney et al. [83], who used realistic models with maximum possible range of changes to determine the climate models generating suitable information about future changes in extreme precipitation in South Asia. Downscaling methods add to the uncertainty of future climate projections [79]. Quantile mapping, which has showed better performance for bias correction of stationary data (Heo et al., 2019) was used in this study to correct the systematic biases of the GCMs. Here, the distribution of observed data is transferred to the projected values. Therefore, the quality of observed data also influences the biases in future climate uncertainty.

The rainfall recorded on the January 8, 2013 (106.7, 89.0, and 81.5 mm of rainfall for Nablus, Tulkarm, and Jenin rain gauges respectively) corresponded to a historical return period of between 1 in 5 (89 mm) to 1 in 10 years (103 mm), whereas a 1 in 100-year rainfall event (RX1day: 148 mm) from historical data (1985–2014) could become 205 mm in the mid-future (2041–2060). We note that a Generalised Extreme Value analysis across current and future time windows would provide a more robust characterisation of extremes, including multi-day events, but this ideally requires a longer observational precipitation record and was beyond the scope of this study. Flood models under a mid-future precipitation scenario (MPI-ESM1-2-HR) suggested a 23 % (4 km^2) greater inundation extent compared to the 2013 event, which could affect over 3000 buildings and 100 km of road network (Fig. 10). In comparison, OCHA [45] reported damage to 1570 houses during the January 213 flood event, although it is not clear if the strong winds associated with the winter storm contributed to this count. Flash flooding affects built infrastructure and causes damage and erosion to cropland. However, ponded water, which was apparent in the 2013 flood and our simulations, presents an opportunity for groundwater recharge. Groundwater aquifers sustain populations and agricultural activity in the West Bank but their recharge is projected to decline with climate warming [84]. Issues with water quality linked to groundwater recharge are also a concern since inadequate waste water management and runoff from agricultural areas is linked to observations of increased nitrate contamination [85,86]. Our flood hazard assessment provides the first high-resolution mapping for the region that can support urban planning and infrastructure development to manage storm water runoff and improve water security. Whilst this analysis acts to bound a range of flood hazard scenarios under current and future climate, future climate scenarios remain uncertain in the models we evaluated.

6. Conclusions

In this study, we used pre- and post-flood satellite imagery from an extreme rainfall event in January 2013 to map the associated inundation extent and impacts in the northern West Bank, Palestine. These extents were used as reference data to evaluate the performance of three flood models and quantify current and future flood hazard. Climate analysis revealed that the January 2013 rainfall corresponded to a historical return period of between 1 in 5 to 1 in 10 years. The patterns of future precipitation in the region are uncertain, although more frequent precipitation extremes are likely to increase the risk of flash flooding. Our analysis showed that a 1 in 100-year rainfall event (RX1day: 148 mm) based on historical data (1985–2014) could become 205 mm in the mid-future (2041–2060), which could cause 23 % (4 km^2) greater inundation compared to the 2013 event. Buildings, the road network, and agricultural land are particularly susceptible to flooding and infrastructure development will be required to manage storm water runoff, particularly where channels intersect the road network. Our study demonstrates the value of high-resolution satellite observations to observe flood extents, which then supports model calibration in data scare regions lacking other hydrological observations. Whilst the physics-based HEC-RAS flood model displayed the best performance, the FastFlood model was able to produce a similar inundation pattern and flood depths over 300 times faster using standard computing resources, which provides greater flexibility for deployment within an urban planning decision support environment.

CRediT authorship contribution statement

C. Scott Watson: Writing – review & editing, Writing – original draft, Visualization, Validation, Software, Project administration, Methodology, Investigation, Formal analysis, Data curation, Conceptualization. **Maggie Creed:** Writing – review & editing, Writing – original draft, Visualization, Software, Resources, Methodology, Investigation, Formal analysis, Conceptualization. **Januka Gyawali:** Writing – review & editing, Writing – original draft, Visualization, Validation, Software, Methodology, Investigation, Formal analysis, Data curation, Conceptualization. **Sameer Shadeed:** Writing – review & editing, Writing – original draft, Methodology, Investigation, Data curation. **Jamal Dabbeek:** Writing – review & editing, Writing – original draft, Data curation, Conceptualization. **Divya L. Subedi:** Writing – review & editing, Writing – original draft, Visualization, Methodology, Formal analysis, Data curation. **Rojina Haiju:** Writing – review & editing, Writing – original draft, Visualization, Methodology, Formal analysis, Data curation.

Financial support

This research has been supported by the UK Research and Innovation (UKRI) Global Challenges Research Fund (GCRF) Urban Disaster Risk Hub (grant no. NE/S009000/1) (Tomorrow's Cities), and the Centre for Observation and Modelling of Earthquakes, Volcanoes and Tectonics (COMET). COMET is a partnership between UK Universities and the British Geological Survey.

Declaration of competing interest

The authors declare that they have no known competing financial interests or personal relationships that could have appeared to influence the work reported in this paper.

Acknowledgments

We thank the Ministry of Local Government (Palestine) for providing topographic data and the Palestine Meteorological Department for providing rainfall records. HAIL-CAESAR modelling was undertaken on ARC4, part of the High Performance Computing facilities at the University of Leeds, UK.

Appendix A. Supplementary data

Supplementary data to this article can be found online at https://doi.org/10.1016/j.ijdrr.2025.105977.

Data availability

The flood model outputs of this study and supporting data will be made available at https://zenodo.org/doi/10.5281/zenodo.13583373.

References

[1] S.-K. Min, X. Zhang, F.W. Zwiers, G.C. Hegerl, Human contribution to more-intense precipitation extremes, Nature 470 (2011) 378–381, https://doi.org/10.1038/nature09763.
[2] P.A. O'Gorman, Precipitation extremes under climate change, Curr. Clim. Change Rep. 1 (2015) 49–59, https://doi.org/10.1007/s40641-015-0009-3.
[3] L. Alfieri, B. Bisselink, F. Dottori, G. Naumann, A. de Roo, P. Salamon, K. Wyser, L. Feyen, Global projections of river flood risk in a warmer world, Earths Future 5 (2017) 171–182, https://doi.org/10.1002/2016EF000485.
[4] B. Jongman, P.J. Ward, J.C.J.H. Aerts, Global exposure to river and coastal flooding: long term trends and changes, Glob. Environ. Change 22 (2012) 823–835, https://doi.org/10.1016/j.gloenvcha.2012.07.004.
[5] B. Tellman, J.A. Sullivan, C. Kuhn, A.J. Kettner, C.S. Doyle, G.R. Brakenridge, T.A. Erickson, D.A. Slayback, Satellite imaging reveals increased proportion of population exposed to floods, Nature 596 (2021) 80–86, https://doi.org/10.1038/s41586-021-03695-w.
[6] Y. Hirabayashi, R. Mahendran, S. Koirala, L. Konoshima, D. Yamazaki, S. Watanabe, H. Kim, S. Kanae, Global flood risk under climate change, Nat. Clim. Change 3 (2013) 816–821, https://doi.org/10.1038/nclimate1911.
[7] L. Slater, G. Villarini, S. Archfield, D. Faulkner, R. Lamb, A. Khouakhi, J. Yin, Global changes in 20-year, 50-year, and 100-year river floods, Geophys. Res. Lett. 48 (2021), https://doi.org/10.1029/2020GL091824 e2020GL091824.
[8] Z.W. Kundzewicz, S. Kanae, S.I. Seneviratne, J. Handmer, N. Nicholls, P. Peduzzi, R. Mechler, L.M. Bouwer, N. Arnell, K. Mach, R. Muir-Wood, G.R. Brakenridge, W. Kron, G. Benito, Y. Honda, K. Takahashi, B. Sherstyukov, Flood risk and climate change: global and regional perspectives, Hydrol. Sci. J. 59 (2014) 1–28, https://doi.org/10.1080/02626667.2013.857411.
[9] K.M. Andreadis, O.E.J. Wing, E. Colven, C.J. Gleason, P.D. Bates, C.M. Brown, Urbanizing the floodplain: global changes of imperviousness in flood-prone areas, Environ. Res. Lett. 17 (2022) 104024, https://doi.org/10.1088/1748-9326/ac9197.
[10] L. Devitt, J. Neal, G. Coxon, J. Savage, T. Wagener, Flood hazard potential reveals global floodplain settlement patterns, Nat. Commun. 14 (2023) 2801, https://doi.org/10.1038/s41467-023-38297-9.
[11] R.Y.L. Shaw, T.S. Cheong, A. Halim, S. Chaturvedi, M. Hashizume, G.E. Insarov, Y. Ishikawa, M. Jafari, A. Kitoh, J. Pulhin, C. Singh, K. Vasant, Z. Zhang, Climate Change 2022 : Impacts, Adaptation and Vulnerability: Working Group II Contribution to the Sixth Assessment Report of the Intergovernmental Panel on Climate Change, first ed., Cambridge University Press, 2023 https://doi.org/10.1017/9781009325844.
[12] R. De Risi, F. Jalayer, F. De Paola, I. Iervolino, M. Giugni, M.E. Topa, E. Mbuya, A. Kyessi, G. Manfredi, P. Gasparini, Flood risk assessment for informal settlements, Nat. Hazards 69 (2013) 1003–1032, https://doi.org/10.1007/s11069-013-0749-0.
[13] W. Kron, Flood risk = hazard • values • vulnerability, Water Int. 30 (2005) 58–68, https://doi.org/10.1080/02508060508691837.
[14] C. Galasso, J. McCloskey, M. Pelling, M. Hope, C.J. Bean, G. Cremen, R. Guragain, U. Hancilar, J. Menoscal, K. Mwang'a, J. Phillips, D. Rush, H. Sinclair, Editorial. Risk-Based, pro-poor urban design and planning for tomorrow's cities, Int. J. Disaster Risk Reduct. 58 (2021), https://doi.org/10.1016/j.ijdrr.2021.102158.
[15] D.P. Poudel, S. Blackburn, R. Manandhar, B. Adhikari, J. Ensor, A. Shrestha, N.P. Timsina, The urban political ecology of 'haphazard urbanisation' and disaster risk creation in the Kathmandu valley, Nepal, Int. J. Disaster Risk Reduct. 96 (2023) 103924, https://doi.org/10.1016/j.ijdrr.2023.103924.
[16] A.J. Cannon, S.R. Sobie, T.Q. Murdock, Bias correction of GCM precipitation by quantile mapping: how well do methods preserve changes in quantiles and extremes? J. Clim. 28 (2015) 6938–6959.
[17] D. Shrestha, D.B. Basnyat, J. Gyawali, M.J. Creed, H.D. Sinclair, B. Golding, M. Muthusamy, S. Shrestha, C.S. Watson, D.L. Subedi, R. Haiju, Rainfall extremes under future climate change with implications for urban flood risk in Kathmandu, Nepal, Int. J. Disaster Risk Reduct. 97 (2023) 103997, https://doi.org/10.1016/j.ijdrr.2023.103997.
[18] L. Hawker, P. Bates, J. Neal, J. Rougier, Perspectives on digital elevation model (DEM) simulation for flood modeling in the absence of a high-accuracy open access global DEM, Front. Earth Sci. 6 (2018), https://doi.org/10.3389/feart.2018.00233.
[19] M. Muthusamy, M.R. Casado, D. Butler, P. Leinster, Understanding the effects of Digital Elevation Model resolution in urban fluvial flood modelling, J. Hydrol. 596 (2021) 126088, https://doi.org/10.1016/j.jhydrol.2021.126088.
[20] C.S. Watson, J. Gyawali, M. Creed, J.R. Elliott, City-scale high-resolution flood models and the role of topographic data: a case study of Kathmandu, Nepal, Geocarto Int. 39 (2024) 2387073, https://doi.org/10.1080/10106049.2024.2387073.
[21] G. Di Baldassarre, G. Schumann, P.D. Bates, A technique for the calibration of hydraulic models using uncertain satellite observations of flood extent, J. Hydrol. 367 (2009) 276–282, https://doi.org/10.1016/j.jhydrol.2009.01.020.
[22] D. Molinari, K.M. De Bruijn, J.T. Castillo-Rodríguez, G.T. Aronica, L.M. Bouwer, Validation of flood risk models: current practice and possible improvements, Int. J. Disaster Risk Reduct. 33 (2019) 441–448, https://doi.org/10.1016/j.ijdrr.2018.10.022.
[23] J. Dabbeek, V. Silva, C. Galasso, A. Smith, Probabilistic earthquake and flood loss assessment in the Middle East, Int. J. Disaster Risk Reduct. 49 (2020) 101662, https://doi.org/10.1016/j.ijdrr.2020.101662.
[24] C.C. Sampson, A.M. Smith, P.D. Bates, J.C. Neal, L. Alfieri, J.E. Freer, A High-Resolution Global Flood Hazard Model, vol. 51, 2015, pp. 7358–7381, https://doi.org/10.1002/2015WR016954.
[25] L.T. Jenkins, M.J. Creed, K. Tarbali, M. Muthusamy, R.Ŝ. Trogrlić, J. Phillips, C.S. Watson, H.D. Sinclair, C. Galasso, J. McCloskey, Physics-based simulations of multiple natural hazards for risk-sensitive planning and decision making in expanding urban regions, Int. J. Disaster Risk Reduct. (2022) 103338, https://doi.org/10.1016/j.ijdrr.2022.103338.
[26] F. McClean, R. Dawson, C. Kilsby, Implications of using global digital elevation models for flood risk analysis in cities, Water Resour. Res. 56 (2020), https://doi.org/10.1029/2020WR028241 e2020WR028241.
[27] M.A. Trigg, C.E. Birch, J.C. Neal, P.D. Bates, A. Smith, C.C. Sampson, D. Yamazaki, Y. Hirabayashi, F. Pappenberger, E. Dutra, P.J. Ward, H.C. Winsemius, P. Salamon, F. Dottori, R. Rudari, M.S. Kappes, A.L. Simpson, G. Hadzilacos, T.J. Fewtrell, The credibility challenge for global fluvial flood risk analysis, Environ. Res. Lett. 11 (2016) 094014, https://doi.org/10.1088/1748-9326/11/9/094014.
[28] G.J. Huffman, D.T. Bolvin, D. Braithwaite, K. Hsu, R. Joyce, C. Kidd, E.J. Nelkin, S. Sorooshian, J. Tan, P. Xie, Algorithm theoretical basis document (ATBD) version 06. NASA global precipitation measurement (GPM) integrated multi-satellitE Retrievals for GPM (IMERG) [online], https://gpm.nasa.gov/resources/documents/algorithm-information/IMERG-V06-ATBD, 2023.

[29] R.K. Pradhan, Y. Markonis, M.R. Vargas Godoy, A. Villalba-Pradas, K.M. Andreadis, E.I. Nikolopoulos, S.M. Papalexiou, A. Rahim, F.J. Tapiador, M. Hanel, Review of GPM IMERG performance: a global perspective, Remote Sens. Environ. 268 (2022) 112754, https://doi.org/10.1016/j.rse.2021.112754.

[30] A. Asadzadeh Jarihani, J.N. Callow, K. Johansen, B. Gouweleeuw, Evaluation of multiple satellite altimetry data for studying inland water bodies and river floods, J. Hydrol. 505 (2013) 78–90, https://doi.org/10.1016/j.jhydrol.2013.09.010.

[31] E. Zakharova, K. Nielsen, G. Kamenev, A. Kouraev, River discharge estimation from radar altimetry: assessment of satellite performance, river scales and methods, J. Hydrol. 583 (2020) 124561, https://doi.org/10.1016/j.jhydrol.2020.124561.

[32] D. Entekhabi, E.G. Njoku, P.E. O'Neill, K.H. Kellogg, W.T. Crow, W.N. Edelstein, J.K. Entin, S.D. Goodman, T.J. Jackson, J. Johnson, J. Kimball, J.R. Piepmeier, R.D. Koster, N. Martin, K.C. McDonald, M. Moghaddam, S. Moran, R. Reichle, J.C. Shi, M.W. Spencer, S.W. Thurman, L. Tsang, J. Van Zyl, The soil moisture active passive (SMAP) mission, Proc. IEEE 98 (2010) 704–716, https://doi.org/10.1109/JPROC.2010.2043918.

[33] K.C. Kornelsen, P. Coulibaly, Advances in soil moisture retrieval from synthetic aperture radar and hydrological applications, J. Hydrol. 476 (2013) 460–489, https://doi.org/10.1016/j.jhydrol.2012.10.044.

[34] F. Cian, M. Marconcini, P. Ceccato, Normalized Difference Flood Index for rapid flood mapping: taking advantage of EO big data, Remote Sens. Environ. 209 (2018) 712–730, https://doi.org/10.1016/j.rse.2018.03.006.

[35] R. Shrestha, L. Di, G. Yu, Y. Shao, L. Kang, B. Zhang, Detection of flood and its impact on crops using NDVI - corn case, in: 2013 Second International Conference on Agro-Geoinformatics (Agro-Geoinformatics), 2013 Second International Conference on Agro-Geoinformatics (Agro-Geoinformatics), 2013, pp. 200–204, https://doi.org/10.1109/Argo-Geoinformatics.2013.6621907.

[36] B. DeVries, C. Huang, J. Armston, W. Huang, J.W. Jones, M.W. Lang, Rapid and robust monitoring of flood events using Sentinel-1 and Landsat data on the Google Earth Engine, Remote Sens. Environ. 240 (2020) 111664, https://doi.org/10.1016/j.rse.2020.111664.

[37] G. Mateo-Garcia, J. Veitch-Michaelis, L. Smith, S.V. Oprea, G. Schumann, Y. Gal, A.G. Baydin, D. Backes, Towards global flood mapping onboard low cost satellites with machine learning, Sci. Rep. 11 (2021) 7249, https://doi.org/10.1038/s41598-021-86650-z.

[38] G.J.-P. Schumann, G.R. Brakenridge, A.J. Kettner, R. Kashif, E. Niebuhr, Assisting flood disaster response with earth observation data and products: a critical assessment, Remote Sens. 10 (2018) 1230, https://doi.org/10.3390/rs10081230.

[39] M. Sapountzis, A. Kastridis, A.P. Kazamias, A. Karagiannidis, P. Nikopoulos, K. Lagouvardos, Utilization and uncertainties of satellite precipitation data in flash flood hydrological analysis in ungauged watersheds, Glob Nest J 23 (2021) 388–399.

[40] G. Cremen, C. Galasso, J. McCloskey, A. Barcena, M. Creed, M.E. Filippi, R. Gentile, L.T. Jenkins, M. Kalaycioglu, E.Y. Mentese, M. Muthusamy, K. Tarbali, R.Ś. Trogrlić, A state-of-the-art decision-support environment for risk-sensitive and pro-poor urban planning and design in Tomorrow's cities, Int. J. Disaster Risk Reduct. 85 (2023) 103400, https://doi.org/10.1016/j.ijdrr.2022.103400.

[41] S. Shadeed, GIS-Based flood hazard mapping in the West Bank, Palestine, -najah univ, J. Res. - Nat. Sci. 33 (2018) 1–22, https://doi.org/10.35552/anujr.a.33.1.1612.

[42] N.F. Asmar, J.O.L. Sim, A. Ghodieh, R. Fauzi, Effect of land Use\Land cover changes on estimated potential runoff in the Nablus mountains watersheds of Palestine: a case study, J. Indian Soc. Remote Sens. 49 (2021) 1067–1080, https://doi.org/10.1007/s12524-020-01278-2.

[43] M.A. Hassan, K. Shahin, B. Klinkenberg, G. McIntyre, M. Diabat, A. Al-Rahman Tamimi, R. Nativ, Palestinian water II: climate change and land use, Geogr. Compass 4 (2010) 139–157, https://doi.org/10.1111/j.1749-8198.2009.00294.x.

[44] O. Hawajri, P. Arcos González, R. Castro Delgado, Natural disaster and complex humanitarian emergencies in the occupied palestinain territories, Emerg. Disaster Rep.- Univ. Oviedo 3 (2016) 4–51.

[45] OCHA, Occupied Palestinian Territory: winter storm situation Report (as of 16 january 2013, 1500 hrs) [online], https://www.ochaopt.org/sites/default/files/ocha_opt_winter_storm_situation_report_16_jan_2013_english.pdf, 2013. (Accessed 24 May 2024).

[46] M.F. Hutchinson, Calculation of hydrologically sound digital elevation models, in: Proceedings of the Third International Symposium on Spatial Data Handling, 1988, pp. 117–133.

[47] C. Nuth, A. Kääb, Co-registration and bias corrections of satellite elevation data sets for quantifying glacier thickness change, Cryosphere 5 (2011) 271–290, https://doi.org/10.1016/10.5194/tc-5-271-2011.

[48] J.B. Lindsay, Whitebox GAT: a case study in geomorphometric analysis, Comput. Geosci. 95 (2016) 75–84, https://doi.org/10.1016/j.cageo.2016.07.003.

[49] S. Leprince, S. Barbot, F. Ayoub, J.P. Avouac, Automatic and precise Orthorectification, coregistration, and Subpixel Correlation of satellite images, application to ground Deformation Measurements, IEEE Trans. Geosci. Rem. Sens. 45 (2007) 1529–1558, https://doi.org/10.1109/TGRS.2006.888937.

[50] N. Pettorelli, J.O. Vik, A. Mysterud, J.-M. Gaillard, C.J. Tucker, N.C. Stenseth, Using the satellite-derived NDVI to assess ecological responses to environmental change, Trends Ecol. Evol. 20 (2005) 503–510, https://doi.org/10.1016/j.tree.2005.05.011.

[51] J.D. Tarpley, S.R. Schneider, R.L. Money, Global vegetation Indices from the NOAA-7 Meteorological satellite, J. Appl. Meteorol. Climatol. 23 (1984) 491–494, https://doi.org/10.1175/1520-0450(1984)023%253C0491:GVIFTN%253E2.0.CO;2.

[52] M.R. Atefi, H. Miura, Detection of flash flood inundated areas using relative difference in NDVI from Sentinel-2 images: a case study of the August 2020 event in Charikar, Afghanistan, Remote Sens. 14 (2022) 3647, https://doi.org/10.3390/rs14153647.

[53] E.S. Miles, C.S. Watson, F. Brun, E. Berthier, M. Esteves, D.J. Quincey, K.E. Miles, B. Hubbard, P. Wagnon, Glacial and geomorphic effects of a supraglacial lake drainage and outburst event, Everest region, Nepal Himalaya, Cryosphere 12 (2018) 3891–3905, https://doi.org/10.5194/tc-12-3891-2018.

[54] R.L. Shreve, Statistical Law of stream numbers, J. Geol. 74 (1966) 17–37, https://doi.org/10.1086/627137.

[55] D. Zanaga, R. Van De Kerchove, D. Daems, W. De Keersmaecker, C. Brockmann, G. Kirches, J. Wevers, O. Cartus, M. Santoro, S. Fritz, ESA WorldCover 10 m 2021 v200. https://doi.org/10.5281/zenodo.7254221, 2021.

[56] Microsoft, Global ML building footprints [online], https://github.com/microsoft/GlobalMLBuildingFootprints, 2024. (Accessed 21 May 2024).

[57] OCHA: State of Palestine - Roads [online]. Accessd 24th May 2024. Available from: https://data.humdata.org/dataset/state-of-palestine-roads, 2021.

[58] G.J. Huffman, E.F. Stocker, D.T. Bolvin, E.J. Nelkin, J. Tan, GPM IMERG final precipitation L3 half hourly 0.1 degree x 0.1 degree V06, Goddard Earth Sci. Data Inf. Serv. Cent. GES DISC Greenbelt MD USA (2019).

[59] M.M. Hamed, M.S. Nashwan, M.S. Shiru, S. Shahid, Comparison between CMIP5 and CMIP6 models over MENA region using historical simulations and future projections, Sustainability 14 (2022) 10375, https://doi.org/10.3390/su141610375.

[60] E. Mesgari, S.A. Hosseini, M.S. Hemmesy, M. Houshyar, L.G. Partoo, Assessment of CMIP6 models' performances and projection of precipitation based on SSP scenarios over the MENAP region, J. Water Clim. Change 13 (2022) 3607–3619, https://doi.org/10.2166/wcc.2022.195.

[61] L. Gudmundsson, J.B. Bremnes, J.E. Haugen, T. Engen-Skaugen, Technical Note: downscaling RCM precipitation to the station scale using statistical transformations – a comparison of methods, Hydrol. Earth Syst. Sci. 16 (2012) 3383–3390, https://doi.org/10.5194/hess-16-3383-2012.

[62] P.C.D. Milly, J. Betancourt, M. Falkenmark, R.M. Hirsch, Z.W. Kundzewicz, D.P. Lettenmaier, R.J. Stouffer, Stationarity is Dead: Whither water management? Science 319 (2008) 573–574, https://doi.org/10.1126/science.1151915.

[63] L.J. Slater, B. Anderson, M. Buechel, S. Dadson, S. Han, S. Harrigan, T. Kelder, K. Kowal, T. Lees, T. Matthews, C. Murphy, R.L. Wilby, Nonstationary weather and water extremes: a review of methods for their detection, attribution, and management, Hydrol. Earth Syst. Sci. 25 (2021) 3897–3935, https://doi.org/10.5194/hess-25-3897-2021.

[64] B. van den Bout, V.G. Jetten, C.J. van Westen, L. Lombardo, A breakthrough in fast flood simulation, Environ. Model. Software 168 (2023) 105787, https://doi.org/10.1016/j.envsoft.2023.105787.

[65] T.J. Coulthard, J.C. Neal, P.D. Bates, J. Ramirez, G.A.M. de Almeida, G.R. Hancock, Integrating the LISFLOOD-FP 2D hydrodynamic model with the CAESAR model: implications for modelling landscape evolution, Earth Surf. Process. Landf. 38 (2013) 1897–1906, https://doi.org/10.1002/esp.3478.

[66] L. Begnudelli, B.F. Sanders, Simulation of the St. Francis Dam-Break flood, J. Eng. Mech. 133 (2007) 1200–1212, https://doi.org/10.1061/(ASCE)0733-9399(2007)133:111200.

[67] T.J. Fewtrell, P.D. Bates, M. Horritt, N.M. Hunter, Evaluating the effect of scale in flood inundation modelling in urban environments, Hydrol. Process. 22 (2008) 5107–5118, https://doi.org/10.1002/hyp.7148.

[68] B. Jamali, P.M. Bach, L. Cunningham, A. Deletic, A Cellular Automata fast flood evaluation (CA-fféé) model, Water Resour. Res. 55 (2019) 4936–4953, https://doi.org/10.1029/2018WR023679.
[69] S. Kabir, S. Patidar, X. Xia, Q. Liang, J. Neal, G. Pender, A deep convolutional neural network model for rapid prediction of fluvial flood inundation, J. Hydrol. 590 (2020) 125481, https://doi.org/10.1016/j.jhydrol.2020.125481.
[70] G. Konapala, S.V. Kumar, S. Khalique Ahmad, Exploring Sentinel-1 and Sentinel-2 diversity for flood inundation mapping using deep learning, ISPRS J. Photogrammetry Remote Sens. 180 (2021) 163–173, https://doi.org/10.1016/j.isprsjprs.2021.08.016.
[71] D. Notti, D. Giordan, F. Caló, A. Pepe, F. Zucca, J.P. Galve, Potential and limitations of open satellite data for flood mapping, Remote Sens. 10 (2018) 1673, https://doi.org/10.3390/rs10111673.
[72] P.A. Arias, N. Bellouin, E. Coppola, R.G. Jones, G. Krinner, J. Marotzke, V. Naik, M.D. Palmer, G.-K. Plattner, J. Rogelj, M. Rojas, J. Sillmann, T. Storelvmo, P. W. Thorne, B. Trewin, K.A. Rao, B. Adhikary, R.P. Allan, K. Armour, G. Bala, R. Barimalala, S. Berger, J.G. Canadell, C. Cassou, A. Cherchi, W. Collins, W. D. Collins, S.L. Connors, S. Corti, F. Cruz, F.J. Dentener, C. Dereczynski, A.D. Luca, A.D. Niang, F.J. Doblas-Reyes, A. Dosio, H. Douville, F. Engelbrecht, V. Eyring, E. Fischer, P. Forster, B. Fox-Kemper, J.S. Fuglestvedt, J.C. Fyfe, N.P. Gillett, L. Goldfarb, I. Gorodetskaya, J.M. Gutierrez, R. Hamdi, E. Hawkins, H. T. Hewitt, P. Hope, A.S. Islam, C. Jones, D.S. Kaufman, R.E. Kopp, Y. Kosaka, J. Kossin, S. Krakovska, J.-Y. Lee, J. Li, T. Mauritsen, T.K. Maycock, M. Meinshausen, S.-K. Min, P.M.S. Monteiro, T. Ngo-Duc, F. Otto, I. Pinto, A. Pirani, K. Raghavan, R. Ranasinghe, A.C. Ruane, L. Ruiz, J.-B. Sallée, B.H. Samset, S. Sathyendranath, S.I. Seneviratne, A.A. Sörensson, S. Szopa, I. Takayabu, A.-M. Tréguier, B. van den Hurk, R. Vautard, K. von Schuckmann, S. Zaehle, X. Zhang, K. Zickfeld, Technical summary, in: Masson-Delmotte, Cambridge University Press, Cambridge, UK, 2021, pp. 33–144. V. P., Zhai, A., Pirani, S. L. and Connors, C. (eds.) Climate Change 2021: The Physical Science Basis: Working Group. Contribution to the Sixth Assessment Report of the Intergovernmental Panel on Climate Change. Cambridge University Press, Cambridge, UK, pp. 33–144., edited by: Masson-Delmotte, V. P., Zhai, A., Pirani, S. L., and Connors, C.
[73] J. Rentschler, M. Salhab, B.A. Jafino, Flood exposure and poverty in 188 countries, Nat. Commun. 13 (2022) 3527, https://doi.org/10.1038/s41467-022-30727-4.
[74] J. Neal, I. Villanueva, N. Wright, T. Willis, T. Fewtrell, P. Bates, How much physical complexity is needed to model flood inundation? Hydrol. Process. 26 (2012) 2264–2282, https://doi.org/10.1002/hyp.8339.
[75] FAO, Climate Smart agriculture Sourcebook [online], https://www.fao.org/climate-smart-agriculture-sourcebook/enabling-frameworks/module-c5-climate-resilience/chapter-c5-4/en/, 2017. (Accessed 12 July 2024).
[76] H. Najafi, P.K. Shrestha, O. Rakovec, H. Apel, S. Vorogushyn, R. Kumar, S. Thober, B. Merz, L. Samaniego, High-resolution impact-based early warning system for riverine flooding, Nat. Commun. 15 (2024) 3726, https://doi.org/10.1038/s41467-024-48065-y.
[77] M.J. Hammond, A.S. Chen, S. Djordjević, D. Butler, O. Mark, Urban flood impact assessment: a state-of-the-art review, Urban Water J. 12 (2015) 14–29, https://doi.org/10.1080/1573062X.2013.857421.
[78] D.I. Smith, Flood damage estimation - a review of urban stage-damage curves and loss functions, WaterSA 20 (1994) 231–238, https://doi.org/10.10520/AJA03784738_1124.
[79] J. Teng, J. Vaze, F.H.S. Chiew, B. Wang, J.-M. Perraud, Estimating the relative uncertainties sourced from GCMs and hydrological models in modeling climate change impact on runoff, J. Hydrometeorol. 13 (2012) 122–139, https://doi.org/10.1175/JHM-D-11-058.1.
[80] A. Ahmadalipour, A. Rana, H. Moradkhani, A. Sharma, Multi-criteria evaluation of CMIP5 GCMs for climate change impact analysis, Theor. Appl. Climatol. 128 (2017) 71–87, https://doi.org/10.1007/s00704-015-1695-4.
[81] A.F. Lutz, H.W. ter Maat, H. Biemans, A.B. Shrestha, P. Wester, W.W. Immerzeel, Selecting representative climate models for climate change impact studies: an advanced envelope-based selection approach, Int. J. Climatol. 36 (2016) 3988–4005, https://doi.org/10.1002/joc.4608.
[82] K. Richardson, Understanding and Quantifying Extreme Precipitation Events in South Asia Part I–Understanding Climate Drivers through Case Studies, 2020.
[83] C.F. McSweeney, R.G. Jones, R.W. Lee, D.P. Rowell, Selecting CMIP5 GCMs for downscaling over multiple regions, Clim. Dyn. 44 (2015) 3237–3260, https://doi.org/10.1007/s00382-014-2418-8.
[84] N. Mizyed, Impacts of climate change on water resources availability and agricultural water Demand in the West Bank, Water Resour. Manag. 23 (2009) 2015–2029, https://doi.org/10.1007/s11269-008-9367-0.
[85] F.M. Anayah, M.N. Almasri, Trends and occurrences of nitrate in the groundwater of the West Bank, Palestine, Appl. Geogr. 29 (2009) 588–601, https://doi.org/10.1016/j.apgeog.2009.01.004.
[86] B. Hejaz, I.A. Al-Khatib, N. Mahmoud, Domestic groundwater quality in the northern governorates of the West Bank, Palestine, J, Environ. Public Health (2020) 6894805, https://doi.org/10.1155/2020/6894805, 2020.